acta orthopaedica belgica, 2026, 92, online-only

doi.org/10.52628/92.3.15544

3D bioprinted porous PLLA implants with dual gene modified BMSCs for osteoarthritis cartilage repair

T. LIU[1], S. ZHANG[2], B. WANG[3], Z. MEI[4], G. XIAO[5], H. HE[4], Y. ZHAO[2], S.-Y. WU[6], Z. YANG[7], K. DU[8], P. LIU[9,10]

[1]School of Biomedicine and Nursing (Shandong Institute of Petroleum and Chemical Technology), Dongying, 257097, PR China; [2]School of Health Science and Engineering, University of Shanghai for Science and Technology, Shanghai 200093, China; [3]Weihai Municipal Hospital, Cheeloo College of Medicine, Shandong University, Weihai 264200, China; [4]Guangzhou Punoshi Biotechnology Co., Ltd., Guangzhou, China; [5]Department of Ecommerce, School of Information Science and Technology, Sanda University, Shanghai 201209, China; [6]Shanghai Sanda University Department of Student Affairs, Shanghai 201209, China; [7]DaLi Bai Autonomous Prefecture People's Hospital, Dali 671000, China; [8]Department of Orthopedics, Shidong Hospital Affiliated to University of Shanghai for Science and Technology, Shanghai 200438, China; [9]Department of Computer, School of Information Science and Technology, Sanda University, Shanghai 201209, China; [10]Department of science and education, Dongying People's Hospital (Dongying Hospital of Shandong Provincial Hospital Group), Dongying 257091, China.

Correspondence at: Dr. Ping Liu, Department of Computer, School of Information Science and Technology, Sanda University, Shanghai 201209, China. E-mail: liupingmedicine@163.com

ABSTRACT

This study evaluated whether three-dimensional (3D) bioprinted spherical, porous poly-L-lactic acid (PLLA) drug-loaded implants, combined with bone marrow mesenchymal stem cells (BMSCs) overexpressing transforming growth factor-β1 (TGF-β1) and interleukin-10 (IL-10), can enhance the repair of osteoarthritis (OA)-related cartilage defects. Rat BMSCs were transduced with lentiviral vectors to achieve dual overexpression of TGF-β1 and IL-10, induced toward chondrogenic differentiation, and assessed for chondrogenic marker expression (COL2A1, SOX-9, and aggrecan). Spherical porous PLLA drug-loaded implants were fabricated by 3D bioprinting and characterized for drug loading, porosity, cytocompatibility, skin sensitization, biodegradation, and in vivo release behavior. Histology, micro-computed tomography (micro-CT), and molecular assays evaluated cartilage repair and subchondral bone remodeling. Dual-gene transduction markedly promoted BMSC chondrogenic differentiation with significant up-regulation of COL2A1, SOX-9, and aggrecan. The PLLA scaffolds exhibited high porosity (88.88 ± 2.87%), meeting biomaterial requirements, showed no evident cytotoxicity or skin sensitization, and achieved a 12-week mass-loss (biodegradation) of 42.65%. In vivo, the combined treatment group displayed superior cartilage regeneration and subchondral bone repair compared with controls, accompanied by increased BMP2 and type II collagen (COL-2) expression. 3D-bioprinted porous PLLA drug-loaded implants combined with TGF-β1/IL-10 dual-gene-transduced BMSCs effectively promote repair of OA cartilage defects, indicating satisfactory biocompatibility and potential for clinical translation.

Keywords: 3D bioprinting, Poly-L-lactic acid, Bone marrow mesenchymal stem cells, Osteoarthritis, Cartilage defect.

INTRODUCTION

Osteoarthritis (OA) is one of the most prevalent degenerative joint disorders, characterized by progressive loss of articular cartilage accompanied by subchondral bone sclerosis and synovitis[1–3]. Once a focal cartilage defect forms, the avascular nature of cartilage and its limited cellular regenerative capacity preclude spontaneous restoration of native structure and function, ultimately leading to joint dysfunction and impaired quality of life[4]. Currently available clinical treatments mainly include autologous chondrocyte implantation, microfracture, periosteal coverage, and stem cell implantation[5-9]. Despite advances in cartilage repair techniques such as autologous chondrocyte implantation, long-term outcomes remain variable. Vanlauwe et al. have elaborated these limitations on relevant clinical studies[44]. Therefore, there is a pressing need for patient-specific implantable strategies that combine cellular therapy with localized drug delivery to enhance cartilage repair.

Three-dimensional (3D) bioprinting, built upon computer-aided design (CAD) and patient imaging, enables precise fabrication of scaffolds that recapitulate the geometry of individual defects[10]. Compared with conventional scaffold-making techniques, 3D bioprinting affords controllable pore architecture,

programmable compositional gradients, and proper customization, and has shown considerable promise in bone and cartilage tissue engineering[11,12]. Poly (lactic acid) (PLA) comprises poly (L-lactic acid) (PLLA), poly (D-lactic acid) (PDLA), and poly (DL-lactic acid) (PDLLA). PLLA offered favorable mechanics, degradability, and processability for 3D-printed scaffolds[13,14]. Nevertheless, single-component scaffolds often lack intrinsic bioactivity and fail to provide sustained local drug release, limiting their efficacy in cartilage regeneration[15].

Successful cartilage repair requires attenuation of inflammation and promotion of chondrogenesis[16]. Transforming growth factor-β1 (TGF-β1) drives the chondrogenic differentiation of bone marrow mesenchymal stem cells (BMSCs) and enhances extracellular matrix synthesis[17], whereas interleukin-10 (IL-10), a potent anti-inflammatory cytokine, mitigates the deleterious effects of an inflammatory microenvironment on regenerating tissues[18]. Seeding defects with BMSCs engineered to overexpress TGF-β1 and IL-10 is thus expected to confer dual pro-regenerative and anti-inflammatory benefits, establishing a local milieu conducive to cartilage repair. Integrating such dual-gene-modified BMSCs with a 3D-bioprinted, drug-loaded controlled-release system could achieve synergistic structural repair, microenvironment modulation, and functional restoration. This composite strategy-merging patient-specific scaffold design, sustained pharmacologic delivery, and gene-modified stem-cell therapy-aims to provide a precise and translational solution for repairing OA-related cartilage defects.

MATERIALS AND METHODS

Cell experiments

Culture and phenotypic screening of BMSCs

Rat BMSCs (iCell, Cat. No. RAT-iCell-s018) were cultured in complete medium in a humidified incubator at 37°C, 5% CO2. When cultures reached 80—95% confluence, cells were passaged using 0.25% trypsin at a split ratio of 1:4-1:6. Cell morphology was examined daily by inverted microscopy (Leica DMI8), and medium was changed every 2-4 days. Cells were washed with phosphate-buffered saline (PBS) for phenotypic characterization and analyzed by flow cytometry using antibodies against CD29, CD44, CD34, CD45, and CD90. The complete medium consisted of DMEM/F12 medium containing 10% fetal bovine serum and 1% penicillin-streptomycin. For flow cytometry, the dilution ratio of CD29, CD44, CD34, CD45 and CD90 antibodies was 1:100, and the detection was performed using BD FACSCanto II flow cytometer.

Lentiviral transduction of TGF-β1 and IL-10

One day before transduction, rBMSCs were seeded to ~70—80% confluence. Concentrated lentiviral particles encoding TGF-β1 and IL-10 were mixed with polyethylenimine (PEI) and incubated at room temperature for 15-30 min; polybrene (hexadimethrine bromide) was optionally added to enhance infection. The mixture was added to cells, and the medium was replaced with fresh complete medium after 6-24 h.

Chondrogenic induction and evaluation

After transduction, cells were cultured for 7-21 days in chondrogenic induction medium containing transforming growth factor-β3 (TGF-β3), bone morphogenetic protein-2 (BMP-2), and insulin-transferrin-selenium (ITS), with regular medium changes and morphological monitoring. Chondrogenic differentiation was assessed by inverted microscopy, Alcian blue staining for glycosaminoglycans (GAGs), and immunostaining for type II collagen (COL-2). Gene expression of COL2A1, SOX-9, and aggrecan was quantified by reverse-transcription quantitative PCR (RT-qPCR) using the ΔΔCt method with GAPDH as the internal control. Primer sequences (5′ to 3′) were: COL2A1: F 5′-CAGCAAGAGCAAGGAGAA-3′, R 5′-GGACAGTAGACGGAGGAA-3′SOX-9: F 5′-ACTCCACCTTCACCTACAT-3′, R 5′-ATCTCAGCAATCGTTACCTT-3′aggrecan: F 5′-TGGATGCCTTGGACACTT-3′, R 5′-GACGATGCTGCTCAGATG-3′GAPDH: F 5′-TTCAACGGCACAGTCAAG-3′, R 5′-TACTCAGCACCAGCATCA-3′. Protein levels were analyzed by Western blot: total protein was quantified by bicinchoninic acid (BCA) assay, separated on 10% SDS-PAGE resolving gels, transferred to polyvinylidene difluoride (PVDF) membranes, blocked with 5% non-fat milk, incubated with primary antibodies overnight at 4°C, followed by secondary antibodies at room temperature for 2 h, and visualized by enhanced chemiluminescence (ECL).

3D-printed PLLA spherical porous drug-loaded implants

The active pharmaceutical ingredient was weighed according to the specified ratio for drug loading, dissolved in a small volume of dichloromethane, and introduced into implants of different shapes (including spheres). The mixture was homogenized, the solvent was gently evaporated with mild heating,

and the samples were dried and weighed. The drug loading across 25 spheres was calculated as shown in Equation (I):

$$\text{Drug loading (\%)} = \frac{(m_2 - m_1)}{m_1} \times 100\% \qquad \text{(I)}$$

where m1 and m2 denote the masses before and after loading, respectively; the mean loading was 0.33 ± 0.02%. Porosity was determined by the ethanol displacement method, where V1 is the initial ethanol volume, V2 is the volume after adding the implant, and V3 is the volume after removing the implant. Porosity was calculated as Equation (II):

$$P(\%) = \frac{V_2 - V_1}{V_2 - V_3} \times 100\% \qquad \text{(II)}$$

yielding 88.88 ± 2.87% for the PLLA spherical porous implants. Surface micro-morphology was examined by scanning electron microscopy (SEM). The PLLA material used in this study had a molecular weight of 100,000 Da and a purity of ≥99%. The 3D printing was performed using 3D Bioplotter® Manufacturer Series with the following parameters: printing temperature of 180°C, nozzle diameter of 0.4 mm, and layer thickness of 0.1 mm. For drug loading, the drug and PLLA were mixed at a ratio of 1:100 (w/w), and homogenized for 30 minutes at room temperature.

Biocompatibility and safety evaluation of PLLA

Cytotoxicity assay

BMSCs were cultured as described above. Spherical porous PLLA drug-loaded implants were extracted at 0.1 g material/10 mL complete medium at 37°C for 36 h, and the extract was sterilized by 0.22 μm filtration. Log-phase BMSCs were adjusted to 5.0-6.0 × 10^4 cells/mL and seeded into 96-well plates at 100 μL/well (~5,000-6,000 cells). After overnight incubation at 37°C, 5% CO_2, supernatants were discarded and cells were rinsed twice with PBS. The wells were then either received as a complete medium (negative control), PLLA extract (test group), or phenol solution 64 g/L (positive control). After 24, 48, 72, and 96 h, 10 μL of Cell Counting Kit-8 (CCK-8) solution was added per well, and incubation continued for 4 h. Absorbance was read at 450 nm (OD 450), and the relative growth rate (RGR) was calculated and cytotoxicity graded according to Supplementary Table (S1) (in Supplementary File).

Skin sensitization test

All animal experiments comply with the principles of animal protection, welfare, and ethics, and meet the relevant regulations on animal welfare and ethics in China. The animal use protocol listed below has been reviewed and approved by the Animal Ethics Committee of Guangdong Second Provincial General Hospital (Approval No. 2025-DW-KZ-098-01). Guinea pigs (both sexes, n = 30) were randomized into a negative control group (normal saline), a test group (PLLA extract), and a positive control group (1% 2,4-dinitrofluorobenzene (DNFB) in acetone: olive oil = 1:1). At 24 h before exposure, dorsal hair within a 2.5 cm × 2.5 cm area was shaved. Sensitization exposures: 0.2 mL of the assigned test article was applied, covered with two layers of filter paper, and occluded with cellophane for 6 h; the procedure was repeated on days 7 and 14. Challenge exposure: 14 days after the final sensitization, the contralateral dorsal site of the same area was prepared and challenged with the corresponding solution under 6 h occlusion. Reactions were assessed immediately, at 24, 48, and 72 h, and scored/classified per Supplementary Table (S2, S3) (in Supplementary File).

Implantation and histological evaluation

Six-week -old rats (~200 g) were allocated by euthanasia time point (2, 6, and 12 weeks; n = 2 per time). After anesthesia, the dorsal hair was shaved and disinfected. A ~2 cm longitudinal skin incision centered on the L5 spinous process; the thoracolumbar fascia was opened, and one implant site was created on each side, ~2.5 cm lateral to the spine. Plasma-sterilized spherical porous PLLA drug-loaded implants were placed on the experimental side, and a blank control was placed contralaterally, followed by layered closure. Gentamicin was administered intraperitoneally for 3 consecutive days postoperatively. Hematoxylin and eosin (H&E) staining was used to evaluate inflammation and fibrous capsule grading according to Table (S4, S5) (in Supplementary File) (GB/T 16175-1996).

Biodegradation and drug-release performance

Implants were placed in 100 mL Erlenmeyer flasks containing pH 7.4 PBS (n = 2 per time point) and incubated on a shaker at 37°C, 80 rpm. Time points were 0, 2, 4, 6, 8, 10, and 12 weeks. Solution pH was recorded weekly. At each time point, samples were blotted to remove surface moisture and weighed to obtain the wet mass (WS), then vacuum-dried at 40°C to constant weight to obtain the dry mass (W_R). Water absorption rate and weight loss rate are calculated according to equations (III) and (IV), respectively:

$$WA(\%)= \frac{(W_S-W_R)}{W_R} \times 100\% \quad (III)$$

$$WL(\%)= \frac{(W_O-W_R)}{W_O} \times 100\% \quad (IV)$$

Where, WA is the water absorption rate; WL is the weight loss rate; W0 is the initial weight of the sample; WS is the weight after liquid absorption; and WR is the weight of the sample after drying at each time point.

Drug release kinetics assay

The drug release behavior of zoledronic acid (ZA) and simvastatin (SIM) from 3D-printed PLLA spherical porous drug-loaded implants was evaluated in vitro. Briefly, 3 replicates of implants (n = 3 per drug) were individually placed in 50 mL centrifuge tubes containing 30 mL of pH 7.4 PBS (simulating the in vivo synovial fluid environment), and incubated in a constant temperature shaker at 37°C, 80 rpm. At predefined time points (1, 3, 7, 14, 21, 28, 35, and 42 days), 5 mL of the release medium was collected, and an equal volume of fresh PBS was added to maintain a constant volume. HPLC detection conditions were as follows: mobile phase consisting of methanol: water = 60:40 (v/v), flow rate of 1.0 mL/min, and column temperature of 30°C. The concentration of ZA in the release medium was determined by high-performance liquid chromatography (HPLC) with a UV detector (detection wavelength: 248 nm), and the concentration of SIM was determined by HPLC with a fluorescence detector (excitation wavelength: 238 nm, emission wavelength: 305 nm). The cumulative release percentage of each drug was calculated according to the following formula:

$$\text{Cumulative release}\ (\%) = (C_n \times V_o + \Sigma C_i \times V_i)/M_o \times 100\%$$

C_n is the concentration of the drug in the release medium at the nth time point, V_o is the initial volume of the release medium, C_i is the concentration of the drug in the collected medium at the ith time point, V_i is the volume of the collected medium at the ith time point, and M_o is the total drug loading of the implant. Three independent experiments were performed, and data were presented as mean ± SD. Statistical analysis was performed to compare the release kinetics of ZA and SIM, with $p < 0.05$ considered statistically significant.

OA cartilage defect model and in vivo evaluation of PLLA implants

Specific pathogen-free (SPF) 6-week-old rats (~200 g) were used to establish an osteochondral defect model. Under anesthesia, a ~1 cm medial parapatellar incision was made to expose the femoral condyle. A defect (2 mm diameter, 1.5 mm depth) was drilled with concurrent saline irrigation for cooling, and the drug-loaded implant was inserted, followed by layered closure. At predefined time points, joints underwent micro-computed tomography (micro-CT) scanning (40 kV, 250 μA, 18 μm resolution) to evaluate bone volume fraction (BV/TV) and bone mineral density (BMD). H&E staining assessed the repair tissue morphology. Western blot detected BMP2, type II collagen (COL-2), and runt-related transcription factor 2 (RUNX2); qPCR quantified related gene expression. Three core control groups were set up in this study: Blank surgery group: Only the OA cartilage defect model was established without implanting any materials or performing cell intervention, which was used to evaluate the impact of the surgery itself on defect repair; Conventional treatment group: 3D-printed PLLA spherical porous scaffolds without drug loading or dual-gene-modified BMSCs seeding were implanted, which was used to compare the repair effect between the simple scaffold and the composite strategy of scaffold + dual-gene-modified BMSCs + dual drugs; Control group: Normal rats without OA model establishment, which was used to provide the baseline of morphology and molecular expression of normal cartilage and bone tissues.

Statistical analysis

Normality and variance homogeneity were tested prior to parametric analyses. Between-group comparisons were performed using one-way analysis of variance (ANOVA) followed by Tukey's post hoc test for multiple comparisons; nonparametric tests (Kruskal-Wallis test followed by Dunn's post hoc test) were used when normality or variance homogeneity assumptions were not met. Data were presented as mean ± standard deviation (SD) for all quantitative analyses, and exact sample sizes (n) per group and per time point for each experiment are specified in the corresponding Results section and figure legends. A two-tailed $p < 0.05$ was considered statistically significant. All statistical analyses were performed using SPSS 26.0 software (IBM Corp., Armonk, NY, USA), and all experiments were independently repeated at least three times unless otherwise specified. The sample size (n value) of each control group (including grouping by time point) was clarified: n=3-6 for each group in in vitro experiments, and n=6 for each group in in vivo experiments, which all met the requirements of statistical tests. The basis for selecting statistical methods was clarified: one-way

analysis of variance (ANOVA) followed by Tukey's post hoc test was used for multiple group comparisons in cell experiments; Kruskal-Wallis test followed by Dunn's post hoc test was used in skin sensitization experiments because some data did not meet the normal distribution. All statistical analyses were performed using SPSS 26.0 software (IBM Corp., Armonk, NY, USA), with a significance level of α=0.05. All experiments were independently repeated at least 3 times to ensure the reliability of the results.

RESULTS

TGF-β1/IL-10 dual-gene transduction markedly enhances chondrogenic differentiation and marker expression in rBMSCs

Flow cytometry confirmed the expected phenotype of rat BMSCs (rBMSCs)- CD29+/CD44+ and CD34-/CD45- (Fig. 1a, b). Lentiviral transduction efficiency for TGF-β1/IL-10 was high, and cells retained a plump morphology with firm adhesion (Fig. 1a, c, d).

After 7-21 days of induction, the dual-gene group exhibited a pronounced chondrogenic phenotype: Alcian blue staining showed increased GAGs deposition, and immunohistochemistry (IHC) revealed strong COL-2 positivity (Fig. 2).

RT-qPCR demonstrated that the mRNA levels of COL2A1, SOX-9, and aggrecan in the dual-gene transduction group were significantly higher than those in the single-gene transduction group and non-transduced control group (all $p < 0.05$, $n = 3$ independent experiments, mean ± SD). Western blot further confirmed that the COL-2 protein level in the dual-gene group was significantly elevated compared with the other two groups ($p < 0.05$, $n = 3$ independent experiments, mean ± SD) (Fig. 3).

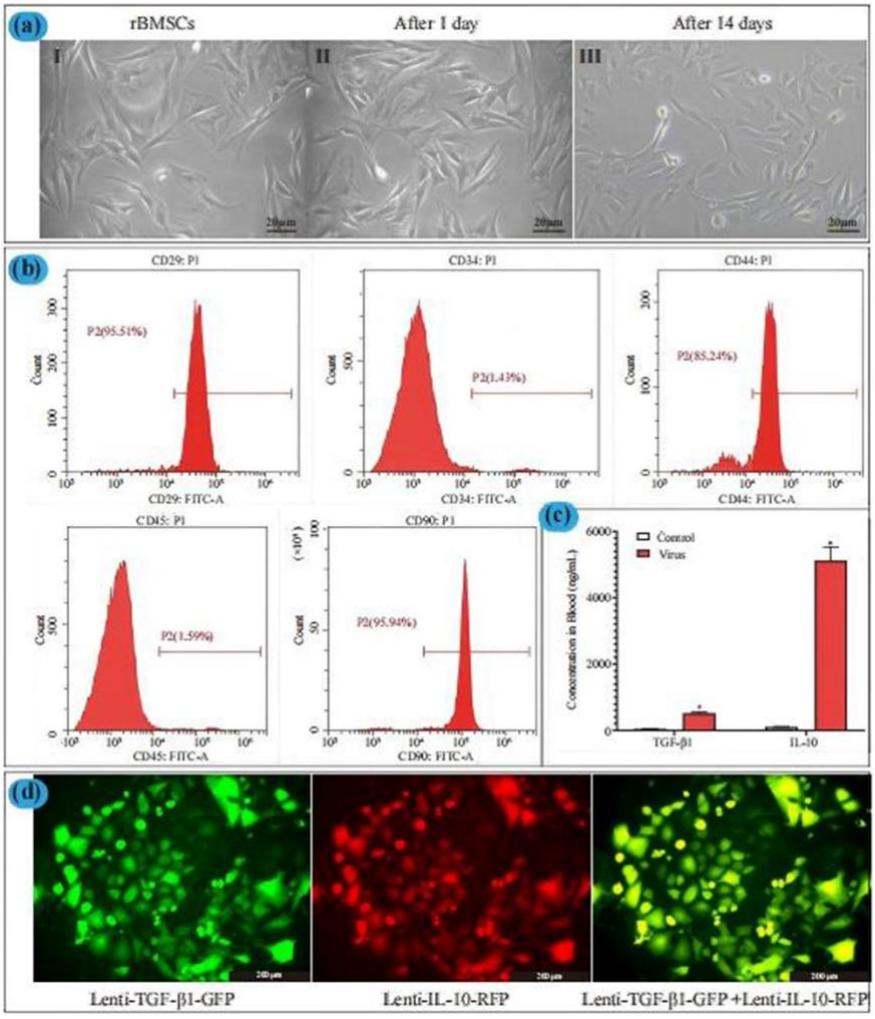

Fig. 1 — (a) I Representative morphology of rBMSCs in culture. II,III Morphology of dual-gene-transduced rBMSCs. (b) Flow-cytometric phenotyping of rBMSCs showing CD29+/CD44+ and CD34-/CD45-profiles. (c) and (d) Establishment of rBMSCs overexpressing TGF-β1 and IL-10.

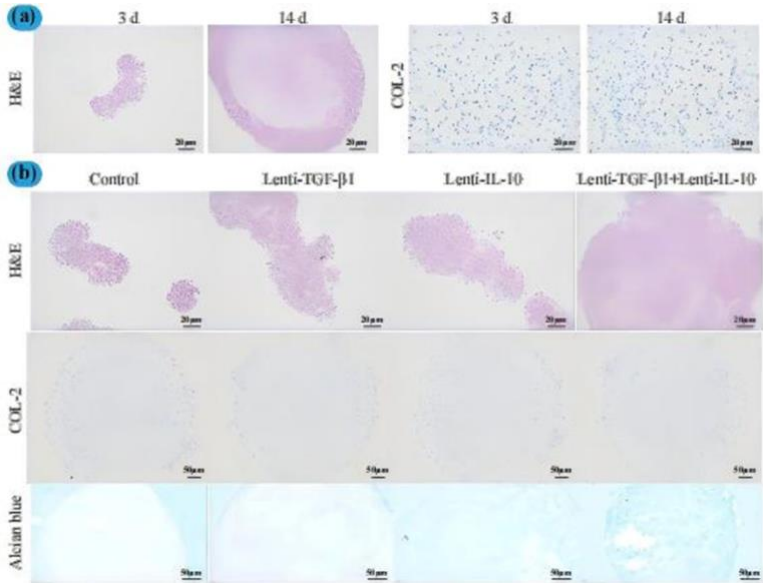

Fig. 2 — (a) HE staining and IHC for COL-2 in cartilage-related tissues/cells. (b) Groupwise comparison by H&E, Alcian blue (GAGs), and COL-2 expression.

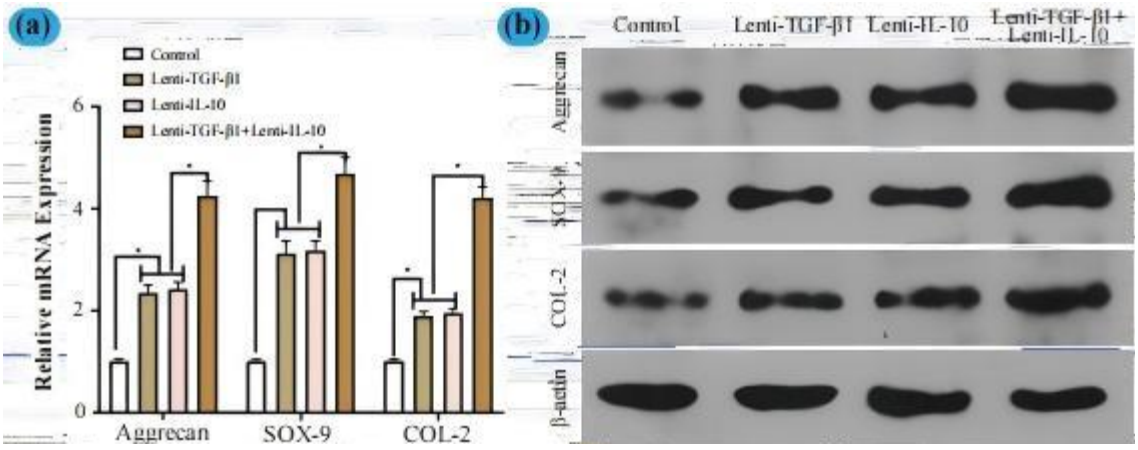

Fig. 3 — Chondrogenic marker expression across groups: RT-qPCR for COL2A1, SOX-9, and aggrecan, and Western blot for COL-2.

Structure and drug-loading characteristics of 3D-printed PLLA spherical porous implants

Gravimetric analysis of 25 spherical implants (n = 25, one implant per sample) showed a mean drug loading of 0.33 ± 0.02% (mean ± SD) (Table I). Ethanol-displacement measurements for porosity were performed in 5 independent samples (n = 5), yielding a porosity of 88.88 ± 2.87% (mean ± SD) (Table II), which meets the commonly accepted > 80% benchmark for biomaterials. The 3D-printed constructs exhibited a uniform spherical porous architecture; SEM revealed homogeneous pore size and a roughened surface favorable for cell adhesion (Fig. 4).

Table I. — Drug loading of spherical porous implants by gravimetric determination.

Pre-Drug Loading	After Drug Loading	Drug Content (%)
0.071	0.108	0.342592593
0.068	0.103	0.339805825
0.069	0.099	0.303030303

Table II. — Porosity of PLLA spherical porous implants.

Number of measurements	V1 (mL)	V2 (mL)	V3 (mL)	Porosity (‰)
1	8.08	8.52	4.11	9.00
2	8.02	8.79	4.15	8.34
3	8.09	8.76	4.22	8.52
4	7.96	8.29	3.92	9.24
5	8.85	9.18	4.58	9.28

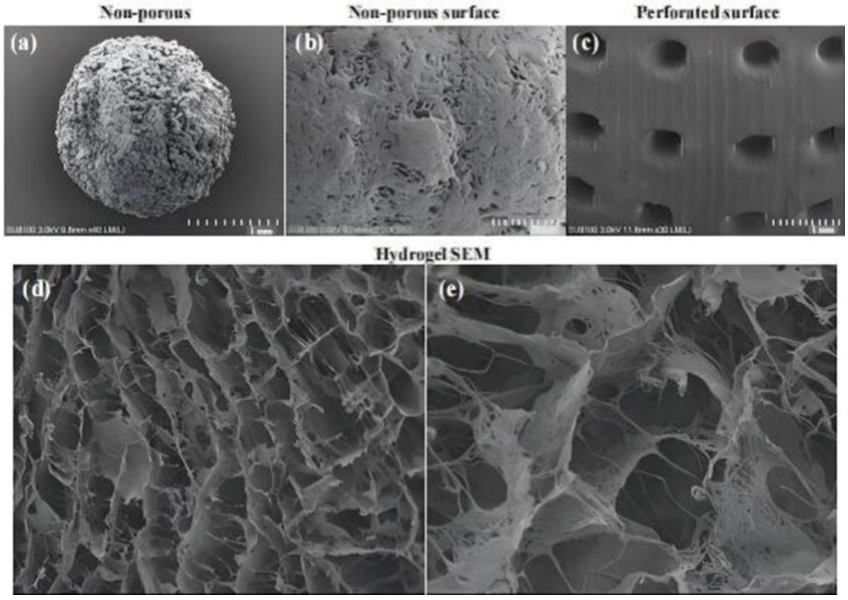

Fig. 4 — SEM micrographs of 3D-printed PLLA spherical porous implants showing uniform pore size and a roughened surface conducive to cell attachment.

Skin sensitization with PLLA spherical drug-loaded implants

The skin sensitization test included 30 guinea pigs, randomized into three groups with 10 animals per group (n = 10 per group). No erythema or edema was observed on the dorsal skin of guinea pigs in the negative control group and the test group (PLLA extract) at any assessment time after sensitization or challenge (mean score = 0, SD = 0) (Table IV). In contrast, the positive control group (DNFB) showed significant erythema and edema at 6, 24, 48, and 72 h after challenge (mean score ± SD: 2.5±0.3/1.5±0.2 at 6 h, 3.3±0.4/2.3±0.3 at 24 h, etc.), with a sensitization rate of 100%. Statistical comparison showed significant differences in skin reaction scores between the positive control group and the other two groups (all $p < 0.05$), while no significant difference was observed between the test group and the negative control group ($p > 0.05$). The sensitization rate of the test group was 0%, and the response was graded as a weak sensitizer, indicating no skin sensitization

Table IV. — Skin reaction scores after sensitization and challenge exposures.

Groups	Skin Reaction Score (Erythema/Edema)									
	First Sensitizing Exposure		Second Sensitizing Exposure		Third Sensitizing Exposure		Challenge Exposure			
	24 h	48 h	24 h	48 h	24 h	48 h	6 h	24 h	48 h	72 h
Negative control group	0/0	0/0	0/0	0/0	0/0	0/0	0/0	0/0	0/0	0/0
Test group	0/0	0/0	0/0	0/0	0/0	0/0	0/0	0/0	0/0	0/0
Positive control group	0/0	0/0	0/0	0/0	0/0	0/0	2.5/1.5	3.3/2.3	2.6/1.7	1.4/1.2

attributable to the PLLA spherical porous drug-loaded implants.

Biocompatibility after implantation study

All animals resumed regular feeding and activity postoperatively; there were no deaths, healing by primary intention, or infections. At 2 weeks, the implant site showed normally colored muscle with mild inflammatory granulation; at 6 weeks, the material was enclosed by a dense fibrous capsule with normal surrounding tissues; at 12 weeks, irregular whitish fibrous tissue formed around the implant with adhesion to muscle. H&E staining demonstrated mild inflammatory reactions and fibrous capsule formation at all time points, consistent with good biocompatibility (Fig. 6). The 2-, 6-, and 12-week time points refer to the dorsal muscle implantation study for biocompatibility assessment, which was a separate experiment from the 48-week cartilage defect repair study.

Controlled biodegradation of PLLA spherical drug-loaded implants

This in vitro degradation study was conducted independently from the in vivo cartilage repair study and lasted 12 weeks. The pH, water absorption, and weight loss were monitored over this period. During PBS incubation, pH remained ~7.4 for the first 4 weeks, began to decline by week 6, and reached 6.23 at week 12 (Fig. 7a). Water absorption increased from ~1% initially to 6.12% by week 8, then plateaued (Fig. 7b). Biodegradation experiments were performed with 2 implants per time point (n = 2 per time point), and weight loss was calculated as mean ± SD. Weight loss rose progressively over time: 5.21 ± 0.83% at 2 weeks,

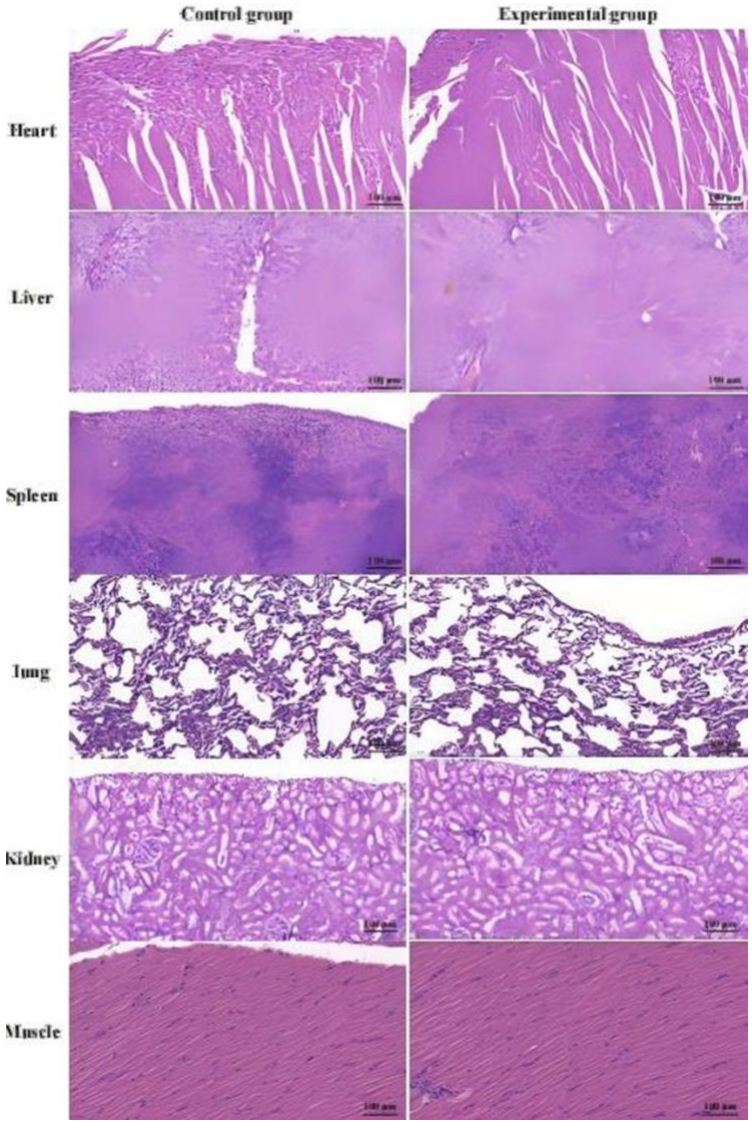

Fig. 6 — Representative histology at implant sites showing tissue compatibility (H&E; 400×).

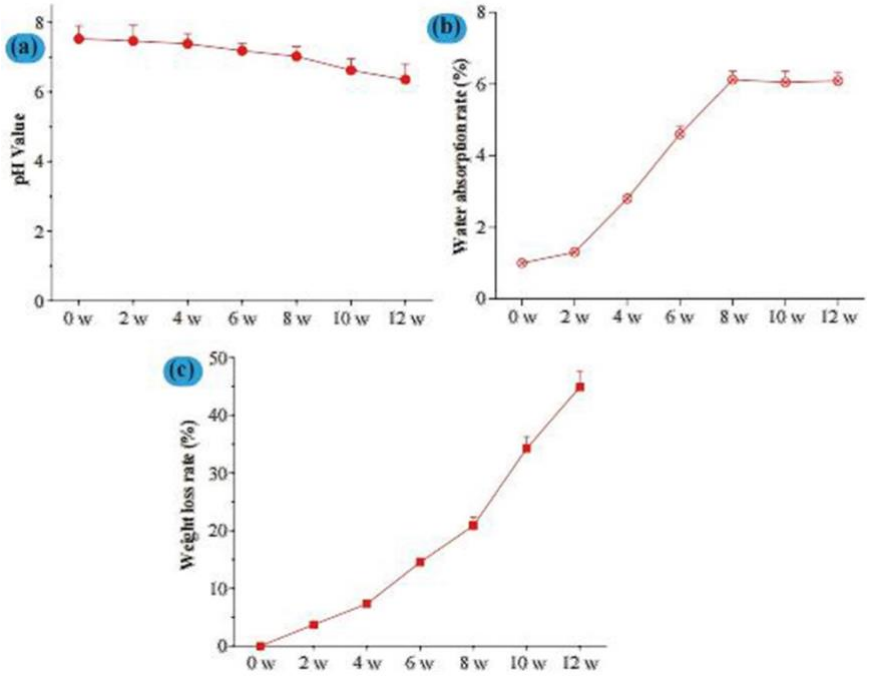

Fig. 7 — (a) Time course of pH during PBS incubation. (b) Water absorption (WA, %) of implants over time. (c) Weight loss (WL, %) of implants over time.

12.35 ± 1.56% at 6 weeks, 28.79 ± 2.14% at 10 weeks, and 42.65 ± 2.87% at 12 weeks (Fig. 7c). Statistical comparison showed significant differences in weight loss between adjacent time points (all $p < 0.05$), indicating appropriate degradability of the material.

Establishment of OA cartilage defect model

Specific pathogen-free (SPF) 6-week-old rats (~200 g) were used to establish an osteochondral defect model. Under anesthesia, a ~1 cm medial parapatellar incision was made to expose the femoral condyle. A defect (2 mm diameter, 1.5 mm depth) was drilled with concurrent saline irrigation for cooling. As shown in Fig. 8, (a) macroscopic photographs and Micro-CT three-dimensional reconstructions of femoral specimens were compared between the Control and OA model groups. Macroscopically, the Control group exhibited normal hind limb morphology without obvious swelling or deformity, while the OA model group displayed apparent joint swelling and abnormal limb posture. Micro-CT analysis revealed that the Control group had intact femoral structure with smooth cortical bone and regularly arranged trabeculae, whereas the OA model group showed irregular cortical thickening, sparse and disordered trabeculae, rough articular surfaces, and osteophyte formation, indicating pathological bone remodeling in osteoarthritis. (b) Hematoxylin and eosin (H&E) staining was performed to confirm the successful establishment of the OA model. The Control group presented normal bone tissue morphology, with dense and orderly trabeculae, clear bone marrow cavity, and uniform cell distribution. In contrast, the OA model group exhibited thinned, fractured, and reduced trabeculae, enlarged bone marrow cavity, inflammatory cell infiltration, and disorganized bone matrix, which collectively verified the successful induction of osteoarthritis lesions.

The successful establishment of the OA cartilage defect model laid a foundation for subsequent evaluation of cartilage regeneration and subchondral bone remodeling outcomes (see Sections 3.8 and 3.9).

Promotion of OA cartilage regeneration by the composite strategy (Cartilage regeneration outcomes)

The core endpoints of cartilage regeneration were defined as: the morphology of repair tissue in cartilage defect area, the deposition of hyaline cartilage-like matrix, and the expression of chondrogenic markers (COL-2, COL2A1, SOX-9, aggrecan, GAGs). To evaluate the effect of the composite strategy (3D-printed PLLA drug-loaded implants + TGF-β1/IL-10 dual-gene-transduced BMSCs) on cartilage regeneration, immunohistochemical (IHC) staining, Western blot, and quantitative real-time polymerase chain reaction (qPCR) were performed to assess the spatiotemporal expression of chondrogenic markers at 4, 16, 32, and 48 weeks post-implantation.

Fig. 8 — (a) Micro-CT of femoral specimens across groups. (b) The confirmation of model establishment (H&E).

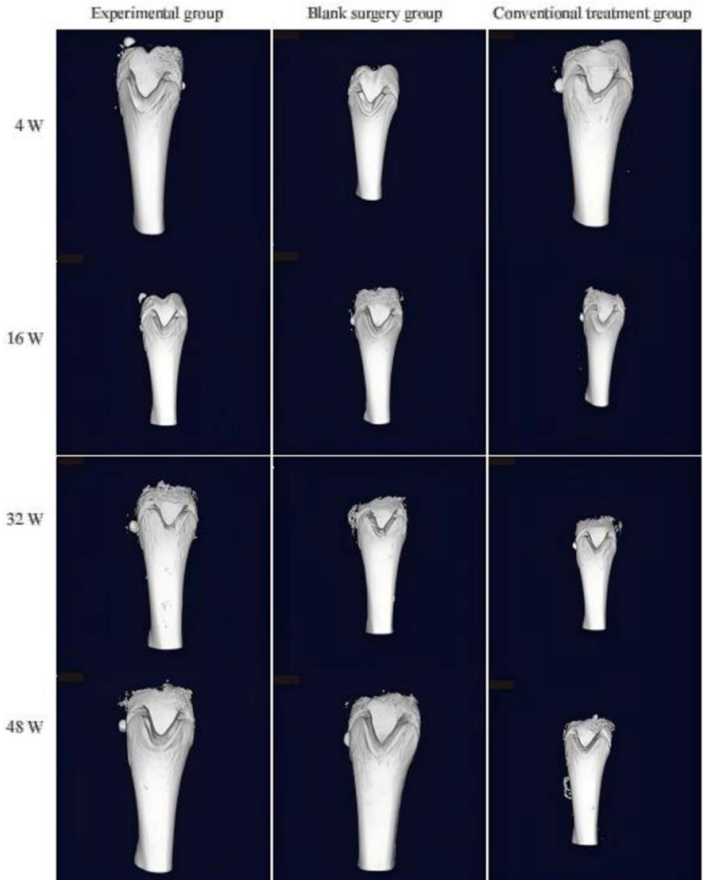

Fig. 9 — Micro-CT evaluation of bone repair (BV/TV and BMD) across groups over time.

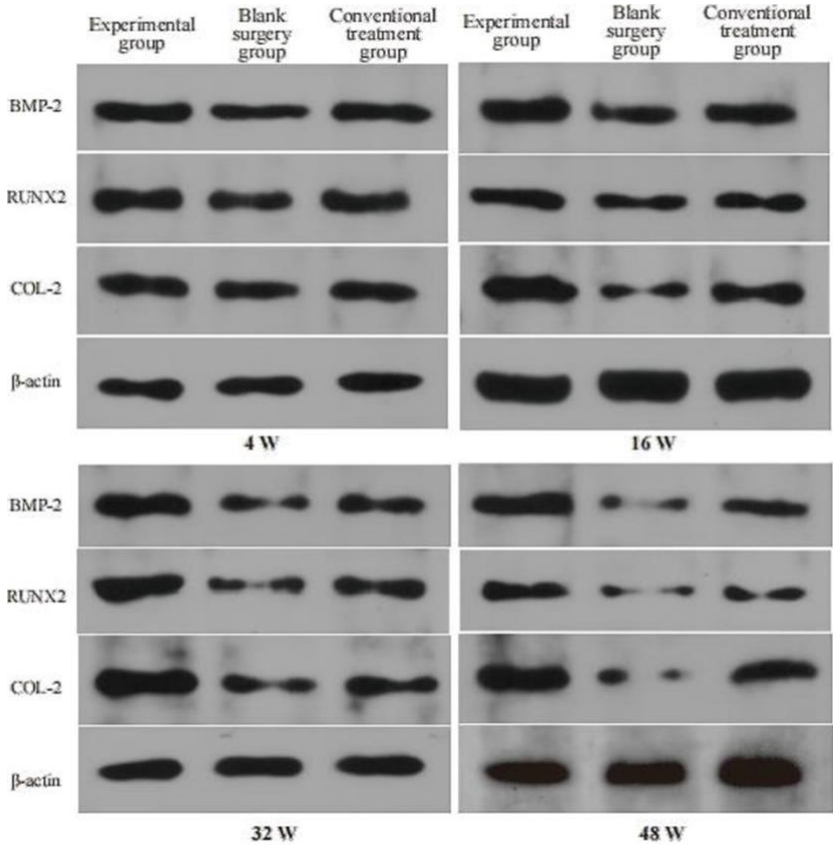

Fig. 10 — Time-dependent changes in protein expression after implantation.

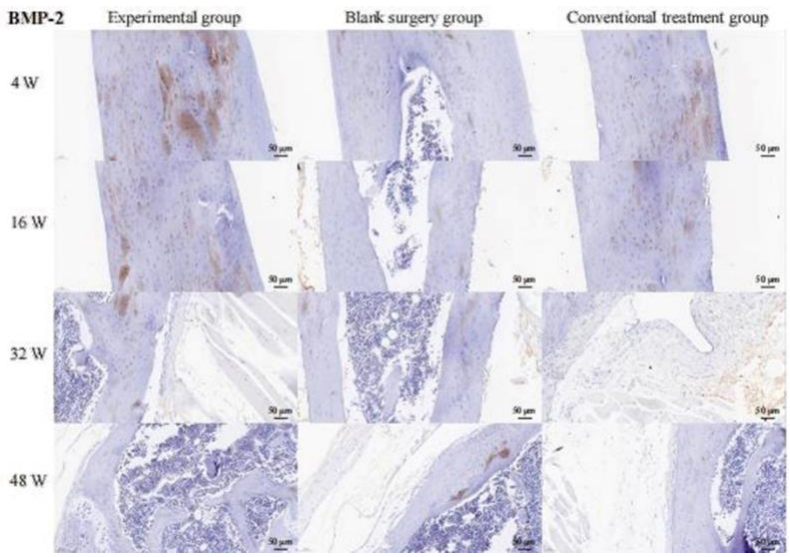

Fig. 11 — Groupwise BMP-2 expression over time.

IHC staining showed progressive upregulation of COL-2 in all groups over time, with the Experimental group displaying the strongest and most sustained positive staining at every time point, followed by the Conventional treatment group, while the Blank surgery group showed the weakest expression (Fig. 12). Western blot analysis revealed that the Experimental group exhibited the highest expression level of COL-2 at all time points, followed by the Conventional treatment group, while the Blank surgery group showed the lowest expression; protein levels in all groups increased over time, peaking at 32–48 weeks, with the Experimental group displaying the most pronounced upregulation (Fig. 10). qPCR

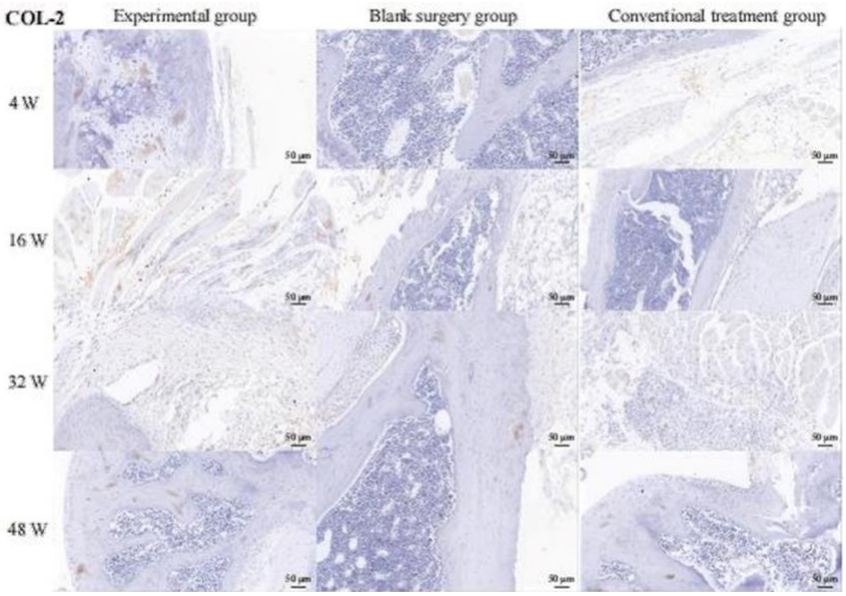

Fig. 12 — Groupwise COL-2 expression over time.

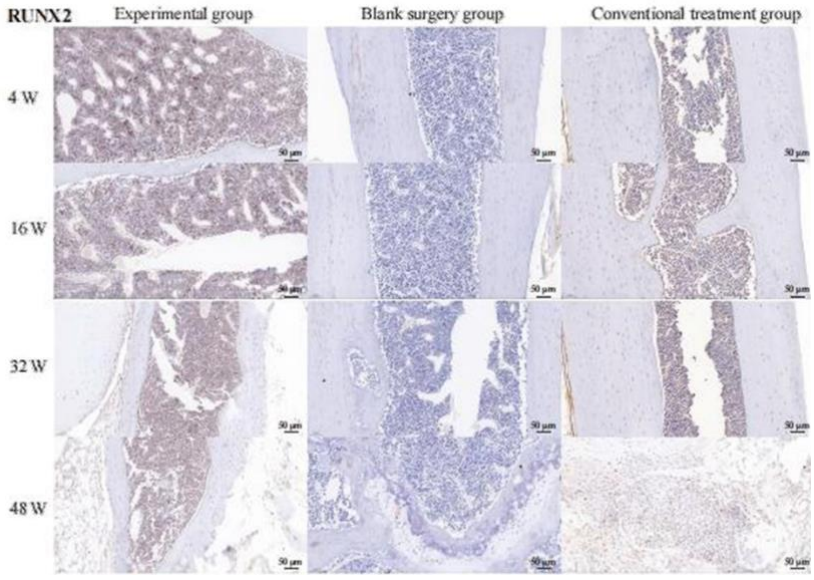

Fig. 13 — Groupwise RUNX2 expression over time.

results closely mirrored the trends observed in protein expression: the Experimental group had the highest relative mRNA expression of COL2A1 at all time points, followed by the Conventional treatment group, while the Blank surgery group showed the lowest levels (Fig. 14).

Histological observation of the cartilage defect area showed that the Experimental group achieved substantial hyaline cartilage-like fill by week 8, with uniform tissue morphology and close integration with the surrounding native cartilage; by week 12, the surface regularity of the repair tissue approached that of normal cartilage, indicating excellent cartilage regeneration effect. In contrast, the Blank surgery group showed only sparse fibrous tissue filling at the defect site, and the Conventional treatment group showed incomplete hyaline cartilage regeneration with uneven matrix deposition.

These results confirmed that the composite strategy significantly promotes cartilage regeneration, which is reflected in the obvious improvement of repair tissue morphology, the significant upregulation of chondrogenic markers, and the formation of hyaline cartilage-like tissue, which fully meets the endpoints of cartilage regeneration research. The promotion of cartilage regeneration by the composite strategy provides

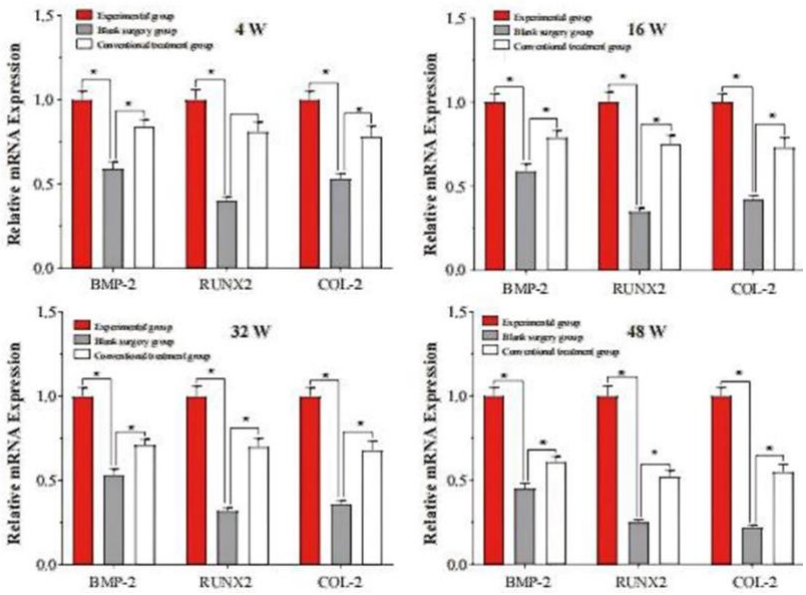

Fig. 14 — Time-dependent changes in related gene expression.

a structural barrier and stable microenvironment for subchondral bone remodeling, and the two processes coordinate with each other to achieve comprehensive osteochondral repair.

Promotion of subchondral bone remodeling by the composite strategy (Subchondral bone remodeling outcomes)

The core endpoints of subchondral bone remodeling were defined as: the structural parameters of subchondral bone (bone volume fraction BV/TV, bone mineral density BMD), the morphology and maturation of trabecular bone, and the expression of osteogenic markers (BMP-2, RUNX2). To evaluate the effect of the composite strategy on subchondral bone remodeling, longitudinal micro-CT analysis, IHC staining, Western blot, and qPCR were performed at 4, 16, 32, and 48 weeks post-implantation.

Micro-CT analysis showed that all groups exhibited significant time-dependent increases in BV/TV and BMD ($n = 6$ per group per time point, mean ± SD, all $p < 0.05$ compared with the same group at 4 weeks). The Experimental group consistently achieved the highest BV/TV and BMD values at all time points, followed by the Conventional treatment group, while the Blank surgery group showed the slowest mineralization and bone mass accumulation (all $p < 0.05$ between groups at the same time point). At 4 weeks, the Experimental group showed extensive early bone formation and active osteogenesis at the defect site; from 16 to 32 weeks, the Experimental group showed the most robust trabecular maturation and host bone integration; by 48 weeks, the Experimental group achieved complete defect closure with dense, well-organized bone structures, whereas the Blank surgery group remained incompletely healed and the Conventional treatment group showed intermediate repair outcomes (Fig. 9).

IHC staining revealed that RUNX2 expression peaked at early time points (4–16 weeks) and then stabilized, with the Experimental group exhibiting the most intense nuclear staining, indicating robust early osteogenic commitment; BMP-2 expression was progressively upregulated over time in all groups, with the Experimental group displaying the strongest positive staining at every time point (Fig. 11, 13). Western blot and qPCR results confirmed that the Experimental group had the highest expression levels of BMP-2 and RUNX2 (protein and mRNA) at all time points, followed by the Conventional treatment group, while the Blank surgery group showed the lowest levels (Fig. 10, 14).

These results confirmed that the composite strategy significantly promotes subchondral bone remodeling, which is reflected in the significant improvement of subchondral bone structural parameters, the maturation and integration of trabecular bone, and the upregulation of osteogenic markers, which fully meets the endpoints of subchondral bone remodeling research. The improvement of subchondral bone structure and mechanical support capacity further promotes the maturation and stability of regenerated cartilage, forming a synergistic repair effect with cartilage regeneration.

Hematoxylin and eosin (H&E) staining was performed to evaluate the histopathological morphology

of major organs (heart, liver, spleen, lung, kidney, and muscle) across all groups (Figure 15).

No obvious morphological abnormalities, inflammatory infiltration, necrosis, or tissue damage were observed in any organ of the Experimental group, Blank surgery group, or Conventional treatment group. All tissues maintained intact structural integrity and normal cellular arrangement, consistent with healthy organ morphology. These findings confirmed the excellent in vivo biosafety of the experimental material, demonstrating no systemic toxic effects or organ damage following implantation.

Drug release kinetics of 3D-printed PLLA spherical porous drug-loaded implants

The in vitro drug release kinetics of ZA and SIM from the 3D-printed PLLA spherical porous implants were quantitatively analyzed, and the cumulative release curves (cumulative release percentage vs. time) are shown in Fig. 16. The release profiles of ZA and SIM exhibited distinct temporal characteristics, consistent with the "temporal staging" hypothesis proposed in this study.

For ZA, an early burst release was observed: the cumulative release percentage reached 45.23 ± 3.12% within the first 3 days, and increased to 68.79 ± 4.56% by day 7, accounting for the majority of the total drug loading. After day 7, the release rate slowed significantly, with a cumulative release percentage of 72.35 ± 5.11% at day 14, and no obvious increase thereafter ($p > 0.05$ compared with day 7). This early burst release pattern is conducive to rapidly inhibiting osteoclast activity and reducing inflammatory responses in the acute phase of cartilage repair.

In contrast, SIM showed a delayed-onset and sustained release pattern: the cumulative release percentage was only 8.67 ± 1.23% at day 7, began to increase gradually from day 14, reached 42.34 ± 3.89% at day 28, and peaked at 65.78 ± 4.22% at day 42. Statistical analysis showed that the cumulative release percentage of SIM at day 14, 28, and 42 was significantly higher than that at day 7 (all $p < 0.05$), indicating a sustained release profile that matches the chondrogenic differentiation window of BMSCs during osteochondral repair.

The release kinetics of ZA and SIM showed significant differences ($p < 0.05$) at all time points except day 42: ZA mainly released in the early stage

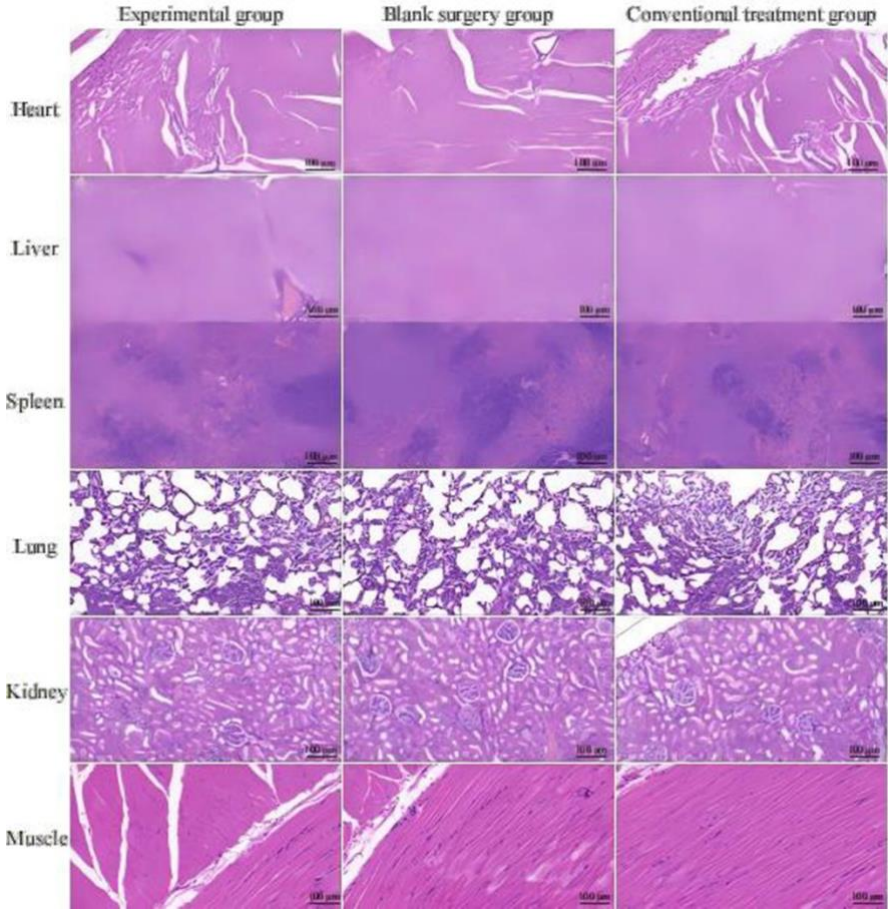

Fig. 15 — H&E of major organs across groups.

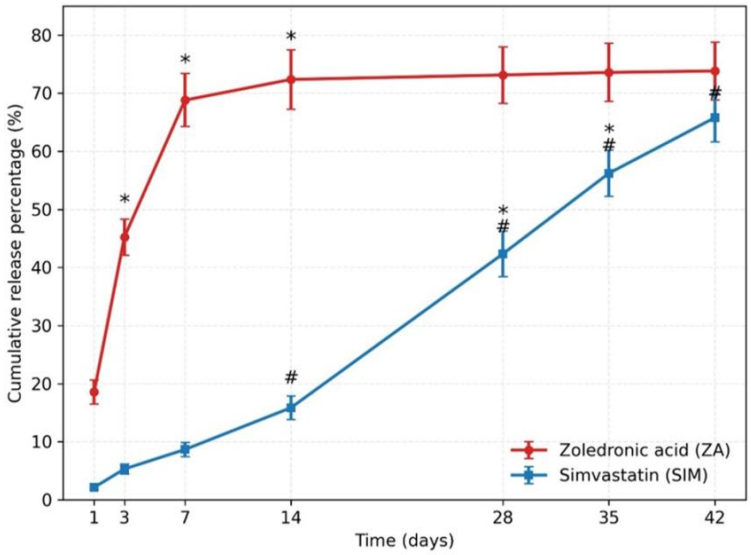

*Fig. 16 — Cumulative release curves of zoledronic acid (ZA) and simvastatin (SIM) from 3D-printed PLLA spherical porous drug-loaded implants in vitro. Data are presented as mean ± SD (n = 3 per drug). *p < 0.05 vs. ZA at the same time point; #p < 0.05 vs. the same drug at day 7.*

(1-7 days) to exert anti-inflammatory effects, while SIM released in the middle and late stages (14-42 days) to promote chondrogenic/osteogenic differentiation, which together form a temporally staged release pattern that is consistent with the immune-to-regeneration sequence of cartilage healing.

DISCUSSION

This study integrated 3D bioprinted degradable PLLA multi-drug implants with BMSCs co-expressing TGF-β1/IL-10, and systematically evaluated their efficacy and mechanisms for repairing OA cartilage defects in vitro and in vivo. It should be noted that the rat osteochondral defect model used in this study is a proof-of-concept model, which is mainly used to initially verify the efficacy of the composite intervention strategy in cartilage repair. This model can simulate local cartilage defects and associated inflammatory responses related to OA, but it cannot fully reproduce the complexity of human OA, especially the chronic inflammatory process and physiological biomechanical loading of human joints. Our results demonstrated advantages across multiple critical dimensions, supporting the potential utility of this composite strategy in tissue engineering and patient-specific therapeutic interventions.

Cartilage regeneration outcomes

The core endpoints of cartilage regeneration evaluated in this study included chondrogenic differentiation capacity, hyaline cartilage-like matrix deposition, and the expression of chondrogenic markers (glycosaminoglycans (GAGs), type II collagen (COL-2), COL2A1, SOX-9, and aggrecan). Using lentiviral vectors to stably introduce TGF-β1 and IL-10 into rabbit BMSCs, we observed during in vitro chondrogenic induction that GAGs deposition, COL-2 expression, and mRNA levels of COL2A1, SOX-9, and aggrecan were all significantly higher in the dual-gene modified group compared with single-gene modified or non-transduced control groups. These data are consistent with previous reports that TGF-β1 activates the SMAD2/3 signaling pathway to up-regulate the expression of cartilage matrix-related genes[19,20]. Consistent with previous studies (References 18, 21), the results of this study suggest that IL-10 may inhibit the expression of inflammatory mediators by down-regulating the NF-κB signaling pathway, thereby reducing the inflammatory damage of the cartilage matrix. The specific regulatory mechanism needs to be further verified by in vitro molecular experiments[18,21]. Our results suggested that the TGF-β1/IL-10 dual-gene combination concurrently sustains a stable chondrogenic phenotype and restrains inflammatory degradation—two key bottlenecks that have long hindered effective cartilage repair. Notably, unlike previous studies in which isolated TGF-β1 overexpression was shown to drive chondrocyte hypertrophy and ectopic ossification[222,23], we observed a transient increase in runt-related transcription factor 2 (RUNX2) expression that later stabilized.

This phenomenon is plausibly attributed to IL-10-mediated modulation of inflammatory signaling and hypertrophic programs, which favors the maintenance of a hyaline cartilage-like phenotype[24]—a critical advantage for long-term cartilage repair outcomes.

The optimized 3D-bioprinted PLLA scaffold also contributed significantly to cartilage regeneration. With a porosity of ~88% and uniform, well-interconnected pores, the scaffold provided a favorable microenvironment for BMSC adhesion, spreading, and matrix secretion, as confirmed by scanning electron microscopy (SEM). Prior research has indicated that porous scaffolds with pore sizes ranging from 100 to 300 μm and high interconnectivity can facilitate nutrient exchange and metabolite diffusion, thereby promoting 3D cell growth and matrix deposition[25-27]. Surface roughness of the scaffold further regulated integrin-mediated signaling pathways (e.g., focal adhesion kinase (FAK) and mitogen-activated protein kinase (MAPK) pathways), enhancing MSC adhesion and chondrogenic lineage commitment[28,29]. Our in vitro data showed uniform BMSC adhesion and abundant matrix secretion, with live-cell staining confirming sustained cell viability—findings concordant with previous reports on the high biocompatibility of PLA-based scaffolds for MSCs[30].

In terms of pharmacology, the temporally staged release of zoledronic acid (ZA) and simvastatin (SIM) from the PLLA scaffold was tailored to support cartilage regeneration. ZA's early burst release (days 3–7) dampened acute inflammation by down-regulating pro-inflammatory mediators such as tumor necrosis factor-α (TNF-α), interleukin-1β (IL-1β), and matrix metalloproteinase-13 (MMP-13)[31-33], creating a favorable microenvironment for chondrogenesis. SIM's delayed-onset, sustained release (2–6 weeks) closely matched the MSC chondrogenic differentiation window[35], up-regulating bone morphogenetic protein-2 (BMP-2) and vascular endothelial growth factor (VEGF) to promote chondrocyte maturation[36,37]. This coordinated release profile aligned with the immune-to-regeneration sequence of cartilage healing[38], translating to substantial hyaline cartilage-like defect filling by week 8 and near-normal surface regularity by week 12 in vivo—clear evidence of effective cartilage regeneration.

Subchondral bone remodeling outcomes

Distinct from cartilage regeneration endpoints, the core endpoints of subchondral bone remodeling evaluated herein included subchondral bone structural parameters (bone volume fraction (BV/TV), bone mineral density (BMD)), trabecular bone morphology and maturation, and the expression of osteogenic markers (BMP-2, RUNX2). The composite strategy exhibited significant efficacy in promoting subchondral bone remodeling, which is critical for long-term cartilage stability and functional recovery.

The PLLA scaffold's porous architecture (88% porosity, well-interconnected pores) provided mechanical support for subchondral bone regeneration while facilitating osteoblast migration and nutrient diffusion. In vivo micro-computed tomography (micro-CT) analysis showed that the composite treatment group achieved significantly higher BV/TV and BMD values at all time points compared with control groups, indicating enhanced bone mass accumulation and mineralization. By week 12, the subchondral plate continuity in the experimental group approached that of normal joints, with dense, well-organized trabecular bone—findings that confirm effective subchondral bone remodeling.

The dual-drug release profile also played a key role in subchondral bone remodeling. ZA's early burst release inhibited osteoclast activity during the acute phase[31-33], limiting excessive subchondral bone resorption and preserving bone structure. Previous studies have shown that ZA can regulate the RANKL/OPG axis in osteoblasts and chondrocytes. Combined with the results of this study that ZA can inhibit osteoclast activity and reduce subchondral bone resorption, it is speculated that ZA may improve the osteochondral interface microenvironment through this axis, and its specific regulatory mechanism needs further in-depth study[34]. SIM's sustained release, meanwhile, up-regulated BMP-2 expression[36,37], promoting osteogenic differentiation of MSCs and trabecular bone maturation. These effects were further supported by the dual-gene modified BMSCs: TGF-β1 enhanced osteogenic differentiation, while IL-10 reduced inflammatory-mediated bone resorption, collectively accelerating subchondral bone repair.

Regarding scaffold degradation, PLLA exhibited typical hydrolytic behavior in pH 7.4 phosphate-buffered saline (PBS), with the pH dropping to 6.23 by week 12 due to lactic acid accumulation—a byproduct of degradation. While a pH below 6.5 can impair MSC proliferation and activate osteoclasts[39,40], we observed no acidification-related inflammation or tissue necrosis in vivo. This was attributed to multiple buffering mechanisms: synovial fluid circulation diluting degradation products[41], the scaffold's high porosity facilitating lactic acid diffusion[42], BMSC-secreted matrix providing additional buffering[43], and the anti-

inflammatory effects of IL-10, TGF-β1, ZA, and SIM mitigating acid-driven detriments. This balanced degradation profile ensured mechanical integrity during subchondral bone remodeling, avoiding premature scaffold collapse and supporting bone regeneration.

Innovations, limitations, and future directions

The innovations of this work are threefold. First, we combined dual-drug controlled release with dual-gene-modified BMSCs within a 3D-bioprinted, patient-specific scaffold, showing potential multilevel coordination among structure, pharmacology, and cells, which requires further verification to confirm the presence and extent of synergistic interactions. Second, we proposed and validated a temporally staged release concept that partitions repair into early inflammation suppression and later pro-differentiation phases. Third, we provided a system-level verification covering structural optimization, drug release, cellular differentiation, and in vivo repair, providing a potential route toward clinical translation that needs further validation. Given the heterogeneity of OA and other cartilage defects, 3D-printed individualized scaffolds can be tailored to lesion geometry, cartilage thickness, and mechanical milieu, and combined with gene/drug delivery for more targeted therapy.

This study has limitations. Small-animal (rat and rabbit) models cannot fully recapitulate human OA's complex biomechanics and pathology; long-term stability of dual-gene expression and potential immune risks warrant further assessment; and drug-release kinetics under high load remain to be clarified. Nevertheless, biosafety and regulatory issues must be considered for lentiviral gene modification. Potential risks include insertional mutagenesis, unstable long-term transgene expression, and host immune responses. Rigorous preclinical safety evaluations and compliance with gene therapy regulatory guidelines and GMP standards will be essential to ensure clinical safety and translation. Another limitation is the lack of comprehensive control groups to dissect the individual contributions of the scaffold, dual-drug release, and dual-gene-modified BMSCs. Although the combined treatment showed beneficial effects, we cannot definitively distinguish the specific role of each component or confirm their synergistic actions. Future investigations using a factorial experimental design with separate groups (scaffold only, drugs only, unmodified BMSCs, etc.) will be needed to clarify their individual and cooperative effects on cartilage repair. Future work should extend observation in large-animal models, employ in-vivo and multimodal imaging to track concurrent cartilage and subchondral reconstruction, and explore new composites with tunable degradation (e.g., PLLA-PLLA-hydroxyapatite) to mitigate acidification and enhance osseous integration. Refining the carrier system to precisely program gene and drug delivery schedules will further advance clinical feasibility and process scale-up. To promote the clinical translation of this composite strategy, future work should first extend the observation to large-animal models (such as rabbits, dogs, or pigs) that have more similar joint anatomy and biomechanical characteristics to humans.

CONCLUSIONS

This study systematically investigated the efficacy and biocompatibility of 3D-bioprinted spherical porous poly-L-lactic acid (PLLA) drug-loaded implants combined with bone marrow mesenchymal stem cells (BMSCs) dual-overexpressing transforming growth factor-β1 (TGF-β1) and interleukin-10 (IL-10) for the repair of osteoarthritis (OA)-related cartilage defects, and the key findings leaded to the following conclusions.

First, lentiviral-mediated dual transduction of TGF-β1 and IL-10 significantly enhances the chondrogenic differentiation potential of rat BMSCs, as evidenced by the marked up-regulation of chondrogenic marker genes (COL2A1, SOX-9, and aggrecan) and proteins (type II collagen, COL-2), as well as increased deposition of glycosaminoglycans (GAGs). This dual-gene modification achieves synergistic effects of promoting chondrogenesis and suppressing inflammation, effectively addressing two critical bottlenecks in cartilage repair and avoiding the chondrocyte hypertrophy associated with single TGF-β1 overexpression.

Second, the 3D-bioprinted spherical porous PLLA drug-loaded implants exhibit excellent structural and functional properties that meet the requirements of biomaterials for cartilage tissue engineering. The scaffolds possessed a high porosity (88.88 ± 2.87%) with uniform, interconnected pores and a rough surface, which facilitates cell adhesion, nutrient exchange, and extracellular matrix deposition. Additionally, the implants demonstrate good biocompatibility, with no evident cytotoxicity or skin sensitization, and undergo controlled biodegradation with a 42.65% mass loss at 12 weeks, accompanied by a manageable acidification profile that does not induce adverse in vivo reactions.

Third, in vivo experiments confirm that the composite strategy of 3D-bioprinted PLLA drug-

loaded implants combined with TGF-β1/IL-10 dual-gene-transduced BMSCs significantly promotes OA-related cartilage defect repair and subchondral bone remodeling. This combination leads to superior hyaline cartilage-like tissue regeneration, increased expression of bone morphogenetic protein 2 (BMP2) and COL-2, and improved bone volume fraction (BV/TV) and bone mineral density (BMD) at the defect site, without causing abnormalities in major organs. Specifically, the composite strategy successfully achieved the predefined endpoints of cartilage regeneration (formation of hyaline cartilage-like tissue, significant upregulation of chondrogenic markers including COL-2 and COL2A1) and subchondral bone remodeling (improvement of bone structural parameters BV/TV and BMD, maturation and integration of trabecular bone, upregulation of osteogenic markers including BMP-2 and RUNX2), and realized the synergistic promotion of the two processes. This further confirms the effectiveness and superiority of the composite strategy in osteochondral repair, and lays a foundation for its subsequent clinical translation.

In summary, the integration of 3D bioprinting, dual-gene-modified BMSCs, and sustained drug release shows potential complementary effects across multiple levels, as evidenced by the improved cartilage repair outcomes observed in our study. These findings suggest that the components may work in a coordinated manner to provide an effective, biocompatible, and patient-specific strategy. Future studies on large-animal models and optimized scaffold composites will further refine this strategy to enhance its long-term efficacy and clinical feasibility. It should be emphasized that the findings of this study are based on a rat proof-of-concept model, which cannot fully simulate the complexity of human OA. Therefore, the clinical translation of this composite strategy requires further validation in large-animal models and under load-bearing conditions, to provide more reliable evidence for its clinical application.

Acknowledgments: Not applicable.

Funding: Not applicable.

Conflict of interests: The authors declare that they have no competing interests.

Authors Contributions: Conceptualization: Tao Liu, Bing Wang
Investigation: Hailin He, Shengwei Zhang, Yisa Zhao, Si-Yuan Wu,
Methodology: Ping Liu, Kewei Du
Formal analysis: Shengwei Zhang, Zibin Yang,
Validation: Zhigang Mei, Hailin He
Data curation: Zhigang Mei, Guohua Xiao
Writing-original draft: Shengwei Zhang, Guohua Xiao
Writing-review & editing: Bing Wang, Zibin Yang
Supervision: Ping Liu, Kewei Du.

Ethics approval and consent to participate: All animal experimental protocols have been reviewed and approved by the Animal Ethics Committee of Guangdong Second Provincial General Hospital (Approval No. 2025-DW-KZ-098-01).

Consent for publication: Not applicable.

REFERENCES

1. Martel-Pelletier J, Barr AJ, Cicuttini FM, et al. Osteoarthritis. Nat Rev Dis Primers. 2016;2(1):16072. doi:10.1038/nrdp.2016.72
2. Molnar V, Matišić V, Kodvanj I, et al. Cytokines and Chemokines Involved in Osteoarthritis Pathogenesis. Int J Mol Sci. 2021;22(17):9208. doi:10.3390/ijms22179208
3. Katz JN, Arant KR, Loeser RF. Diagnosis and Treatment of Hip and Knee Osteoarthritis: A Review. JAMA. 2021;325(6):568-578. doi:10.1001/jama.2020.22171
4. Sophia Fox AJ, Bedi A, Rodeo SA. The Basic Science of Articular Cartilage: Structure, Composition, and Function. Sports Health. 2009;1(6):461-468. doi:10.1177/1941738109350438
5. Yoon KH, Lee J, Park JY. Costal Chondrocyte–Derived Pellet-Type Autologous Chondrocyte Implantation Versus Microfracture for the Treatment of Articular Cartilage Defects: A 5-Year Follow-up of a Prospective Randomized Trial. Am J Sports Med. 2024;52(2):362-367. doi:10.1177/03635465231222797
6. Na Y, Shi Y, Liu W, et al. Is implantation of autologous chondrocytes superior to microfracture for articular-cartilage defects of the knee? A systematic review of 5-year follow-up data. Int J Surg. 2019;68:56-62. doi:10.1016/j.ijsu.2019.06.007
7. Knutsen G, Drogset JO, Engebretsen L, et al. A Randomized Multicenter Trial Comparing Autologous Chondrocyte Implantation with Microfracture: Long-Term Follow-up at 14 to 15 Years. J Bone Joint Surg. 2016;98(16):1332. doi:10.2106/JBJS.15.01208
8. Saris DBF, Vanlauwe J, Victor J, et al. Treatment of Symptomatic Cartilage Defects of the Knee: Characterized Chondrocyte Implantation Results in Better Clinical Outcome at 36 Months in a Randomized Trial Compared to Microfracture. Am J Sports Med. 2009;37(1_suppl):10-19. doi:10.1177/0363546509350694
9. Brittberg M, Lindahl A, Nilsson A, Ohlsson C, Isaksson O, Peterson L. Treatment of Deep Cartilage Defects in the Knee with Autologous Chondrocyte Transplantation. New Engl J Med. 1994;331(14):889-895. doi:10.1056/NEJM199410063311401
10. Mikaeeli Kangarshahi B, Naghib SM, Rabiee N. 3D printing and computer-aided design techniques for drug delivery scaffolds in tissue engineering. Expert Opin Drug Del. 2024;21(11):1615-1636. doi:10.1080/17425247.2024.2409913
11. Zhang H, Wang M, Wu R, et al. From materials to clinical use: advances in 3D-printed scaffolds for cartilage tissue engineering. Phys Chem Chem Phys. 2023;25(36):24244-24263. doi:10.1039/D3CP00921A
12. Kelly CN, Miller AT, Hollister SJ, Guldberg RE, Gall K. Design and Structure–Function Characterization of 3D Printed Synthetic Porous Biomaterials for Tissue Engineering. Adv Healthc Mater. 2018;7(7):1701095. doi:10.1002/adhm.201701095

13. Li Z, Huang Q, Luo C, et al. 3D-printed poly (L-lactic acid) Haversian bone scaffold with microspherulitic surface and biocompatibilities. Int J Biol Macromol. 2025;318:145289. doi:10.1016/j.ijbiomac.2025.145289
14. Capuana E, Lopresti F, Ceraulo M, La Carrubba V. Poly-l-Lactic Acid (PLLA)-Based Biomaterials for Regenerative Medicine: A Review on Processing and Applications. Polymers. 2022;14(6):1153. doi:10.3390/polym14061153
15. Echeverria Molina MI, Malollari KG, Komvopoulos K. Design Challenges in Polymeric Scaffolds for Tissue Engineering. Front Bioeng Biotechnol. 2021;9. doi:10.3389/fbioe.2021.617141
16. Choi MC, Jo J, Park J, Kang HK, Park Y. NF-κB Signaling Pathways in Osteoarthritic Cartilage Destruction. Cells. 2019;8(7):734. doi:10.3390/cells8070734
17. Xia P, Wang X, Qu Y, et al. TGF-β1-induced chondrogenesis of bone marrow mesenchymal stem cells is promoted by low-intensity pulsed ultrasound through the integrin-mTOR signaling pathway. Stem Cell Res Ther. 2017;8(1):281. doi:10.1186/s13287-017-0733-9
18. van Helvoort EM, van der Heijden E, van Roon J a. G, Eijkelkamp N, Mastbergen SC. The Role of Interleukin-4 and Interleukin-10 in Osteoarthritic Joint Disease: A Systematic Narrative Review. Cartilage. 2022;13(2):19476035221098167. doi:10.1177/19476035221098167
19. Yu P, Duan L, Yan Z, Li J, Cai DZ. RADA-16-based Self-assembled Peptide Nanofiber Scaffolds Loaded with TGF-β1 Enhance the Chondrogenic Differentiation Potential of BMSCs In vitro. Curr Stem Cell Res T. 19(2):257-266. doi:10.2174/1574888X18666230316112847
20. Zhang T, Wen F, Wu Y, et al. Cross-talk between TGF-beta/SMAD and integrin signaling pathways in regulating hypertrophy of mesenchymal stem cell chondrogenesis under deferral dynamic compression. Biomaterials. 2015;38:72-85. doi:10.1016/j.biomaterials.2014.10.010
21. Carneiro NVQ, Silva HBFD, Silva RRD, et al. Sambucus australis Modulates Inflammatory Response via Inhibition of Nuclear Factor Kappa B (NF-kB) in vitro. An Acad Bras Ciênc. 2019;91:e20170831. doi:10.1590/0001-3765201920170831
22. Wu M, Wu S, Chen W, Li YP. The roles and regulatory mechanisms of TGF-β and BMP signaling in bone and cartilage development, homeostasis and disease. Cell Res. 2024;34(2):101-123. doi:10.1038/s41422-023-00918-9
23. Herberg S, Varghai D, Cheng Y, et al. High-density human mesenchymal stem cell rings with spatiotemporally-controlled morphogen presentation as building blocks for engineering bone diaphyseal tissue. Nanotheranostics. 2018;2(2):128-143. doi:10.7150/ntno.23354
24. Zhang J, Rong Y, Luo C, Cui W. Bone marrow mesenchymal stem cell-derived exosomes prevent osteoarthritis by regulating synovial macrophage polarization. Aging. 2020;12(24):25138-25152. doi:10.18632/aging.104110
25. Matsiko A, Gleeson JP, O'Brien FJ. Scaffold Mean Pore Size Influences Mesenchymal Stem Cell Chondrogenic Differentiation and Matrix Deposition. Tissue Eng Pt A. 2015;21(3-4):486-497. doi:10.1089/ten.tea.2013.0545
26. Zhang Q, Lu H, Kawazoe N, Chen G. Pore size effect of collagen scaffolds on cartilage regeneration. Acta Biomaterialia. 2014;10(5):2005-2013. doi:10.1016/j.actbio.2013.12.042
27. Cohen DJ, Van Duyn CM, Deng J, et al. Bone Marrow Stromal Cells Generate a Pro-Healing Inflammasome When Cultured on Titanium–Aluminum–Vanadium Surfaces with Microscale/Nanoscale Structural Features. Biomimetics. 2025;10(1):66. doi:10.3390/biomimetics10010066
28. Lien SM, Ko LY, Huang TJ. Effect of pore size on ECM secretion and cell growth in gelatin scaffold for articular cartilage tissue engineering. Acta Biomater. 2009;5(2):670-679. doi:10.1016/j.actbio.2008.09.020
29. [Niu H, Lin D, Tang W, et al. Surface Topography Regulates Osteogenic Differentiation of MSCs via Crosstalk between FAK/MAPK and ILK/β-Catenin Pathways in a Hierarchically Porous Environment. ACS Biomater Sci Eng. 2017;3(12):3161-3175. doi:10.1021/acsbiomaterials.7b00315
30. Kwon H, Sun L, Cairns DM, et al. The influence of scaffold material on chondrocytes under inflammatory conditions. Acta Biomater. 2013;9(5):6563-6575. doi:10.1016/j.actbio.2013.01.004
31. Hsieh MK, Wang CY, Kao FC, et al. Local application of zoledronate inhibits early bone resorption and promotes bone formation. JBMR Plus. 2024;8(5):ziae031. doi:10.1093/jbmrpl/ziae031
32. Huang XL, Huang LY, Cheng YT, et al. Zoledronic acid inhibits osteoclast differentiation and function through the regulation of NF-κB and JNK signalling pathways. Int J Mol Med. 2019;44(2):582-592. doi:10.3892/ijmm.2019.4207
33. Li G, Zhang L, Wang L, et al. Dual modulation of bone formation and resorption with zoledronic acid-loaded biodegradable magnesium alloy implants improves osteoporotic fracture healing: An in vitro and in vivo study. Acta Biomater. 2018;65:486-500. doi:10.1016/j.actbio.2017.10.033
34. Wang B, Zhan Y, Yan L, Hao D. How zoledronic acid improves osteoporosis by acting on osteoclasts. Front Pharmacol. 2022;13. doi:10.3389/fphar.2022.961941
35. Al-Baadani MA, Xu L, Cai K, et al. Preparation of co-electrospinning membrane loaded with simvastatin and substance P to accelerate bone regeneration by promoting cell homing, angiogenesis and osteogenesis. Mater Today Bio. 2023;21:100692. doi:10.1016/j.mtbio.2023.100692
36. Wu SC, Chang CH, Chang LH, et al. Simvastatin Enhances the Chondrogenesis But Not the Osteogenesis of Adipose-Derived Stem Cells in a Hyaluronan Microenvironment. Biomedicines. 2021;9(5):559. doi:10.3390/biomedicines9050559
37. Terabe K, Takahashi N, Cobb M, Askew EB, Knudson CB, Knudson W. Simvastatin promotes restoration of chondrocyte morphology and phenotype. Arch Biochem Biophys. 2019;665:1-11. doi:10.1016/j.abb.2019.01.038
38. Quarterman JC, Phruttiwanichakun P, Fredericks DC, Salem AK. Zoledronic Acid Implant Coating Results in Local Medullary Bone Growth. Mol Pharmaceutics. 2022;19(12):4654-4664. doi:10.1021/acs.molpharmaceut.2c00644
39. Krieger NS, Frick KK, Bushinsky DA. Mechanism of acid-induced bone resorption. Curr Opin Nephrol Hy. 2004;13(4):423. doi:10.1097/01.mnh.0000133975.32559.6b
40. Gong S, Ma J, Tian A, Lang S, Luo Z, Ma X. Effects and mechanisms of microenvironmental acidosis on osteoclast biology. BioSci Trends. 2022;16(1):58-72. doi:10.5582/bst.2021.01357
41. Hasnain S, Abbas I, Al-Atawi NO, Saqib M, Afzaal MF, Mashat DS. Knee synovial fluid flow and heat transfer, a power law model. Sci Rep. 2023;13(1):18184. doi:10.1038/s41598-023-44482-z
42. Sasikumar SC, Goswami U, Raichur AM. Mucin-Based Dual Cross-Linkable IPN Hydrogel Bioink for 3D Bioprinting and Cartilage Tissue Engineering. ACS Appl Bio Mater. 2025;8(2):1186-1200. doi:10.1021/acsabm.4c01505
43. Lunyak VV, Amaro-Ortiz A, Gaur M. Mesenchymal Stem Cells Secretory Responses: Senescence Messaging Secretome and Immunomodulation Perspective. Front Genet. 2017;8. doi:10.3389/fgene.2017.00220
44. Vanlauwe J, Almqvist F, Bellemans J, Huskin JP, Verdonk R, Victor J. Repair of symptomatic cartilage lesions of the knee: the place of autologous chondrocyte implantation. Acta Orthop Belg. 2007 Apr;73(2):145-58.

Supplementary table I. — Cytotoxicity rating criteria.

Cytotoxicity grade	Relative Growth Rate (RGR)%
Level 0	≥100
Level 1	75~99
Level 2	50~74
Level 3	25~49
Level 4	1~24
Level 5	0

Supplementary table II. — Skin allergic reaction rating scale.

Skin reaction		Score
Erythema formation	No erythema	0
	Mild erythema	1
	Moderate erythema	2
	Severe erythema	3
	Edematous erythema	4
Edema formation	No edema	0
	Mild edema	1
	Moderate edema	2
	Severe edema	3

Supplementary table III. — Classification of sensitization levels.

Sensitization rate (%)	Reaction intensity
0—10	Weak sensitization
20—30	Mild sensitization
40—60	Moderate sensitization
70—80	Highly allergenic
90—100	Extremely allergenic
Reaction average = (Total score for erythema formation + Total score for edema formation)/Total number of animals. Sensitization rate (%) = The number of animals with skin erythema or edema/The total number of test animals × 100.	

Supplementary table IV. — Grading of inflammatory response severity.

Grading	Degree of inflammatory response
I	Only a very small amount of lymphoid tissue was seen
II	A small amount of lymphoid tissue can be seen
III	A small amount of neutrophil and lymphocyte infiltration and giant cell response can be observed
IV	Inflammatory tissue responses dominated by neutrophils can be observed, and phagocytes can also be seen

Supplementary table V. — Grading of fibrous capsule cavities.

Grading	Degree of inflammatory response
I	Thickness of the capsule wall <0.03 mm, no continued hyperplasia
II	The fibrotic cyst wall is dense, and its thickness is thinner than during the initial formation stage
III	Fibroblasts and collagen fibers have appeared around, and a fibrous cystic cavity structure has already been formed
IV	Small blood vessels and fibroblast proliferation can be seen around, and a loose cyst wall can be observed